Materials Research Express

PAPER

Spark plasma sintering of Inconel 738LC: densification and microstructural characteristics

Materials Research Express

PAPER

Spark plasma sintering of Inconel 738LC: densification and microstructural characteristics

RECEIVED
3 July 2019

REVISED
21 August 2019

ACCEPTED FOR PUBLICATION
10 September 2019

PUBLISHED
20 September 2019

O F Ogunbiyi[1], E R Sadiku[2], T Jamiru[1], O T Adesina[1] and L W Beneke[1]

[1] Department of Mechanical Engineering, Mechatronics and Industrial Design, Tshwane University of Technology, Pretoria, South Africa
[2] Institute for NanoEngineering Research (INER) and Department of Chemical, Metallurgical and Materials Engineering, Tshwane University of Technology, Pretoria, South Africa

E-mail: olugbengaogunbiyi@gmail.com

Keywords: spark plasma sintering, IN738LC, microstructure, densification, hardness

Abstract

The optimization of sintering temperature in the production of nickel-based superalloy was investigated. Mixed elemental powders of Inconel 738LC superalloy was fabricated at different sintering temperature ranging between 900 and 1200 °C, with a heating rate of 100 °C min^{-1}, pressure of 50 MPa and 5 min holding time. The microstructures, phase analyses, densification and microhardness tests were conducted by using scanning electron microscopy (SEM), Energy dispersive spectroscopy (EDS), x-ray Diffraction (XRD), polarized optical microscope (POM), micro-hardness testing machine, and Archimedes' method respectively. Results revealed the formation of intermetallic phases in the microstructure, irrespective of the sintering temperature. The relative density increased with increasing sintering temperature, as the highest relative density of 98.4% was attained at 1200 °C and with a corresponding microhardness value of 362.25 Hv. There was a marginal decrease in grain size with increasing temperature, thereby resulted in reduced grain growth. This implies that the SPS technology is appropriate for the fabrication of nickel-based superalloy.

1. Introduction

The dynamic processes involved in the operation of a gas power plant, more importantly, a turbine system, necessitated the use of engineering materials that have excellent structural stability when in service. Due to the high-temperature working conditions of a turbine, materials of excellent mechanical properties and high-temperature strength are required for its part production. Hence, Inconel 738 low carbon (IN738LC) superalloy is considered suitable for this purpose. IN738LC superalloy, which is a nickel-based superalloy, have excellent mechanical properties, good corrosion-oxidation resistance strength and good structural stability properties at high temperatures [1–4]. Nickel-based superalloys are generally difficult to manufacture due to the combination of different elements in their composition. However, selection of key elements in the right proportion has helped to improve strength of the superalloys and aided their stability at high temperature (650 °C) working conditions. Superalloys are used for various components in a turbine system, which include turbine inlet nozzle, turbine blades, compressor and other high temperature structural components within the system [5]. Other area of applications includes, rocket motor, aerospace engine, pumps, tooling materials and nuclear reactors [6, 7]. On many occasions, the assessment of the economic viability and efficiency of a turbine power plant is usually informed from the turbine flexibility to accommodate potential increase in the operating temperature, due to demand for energy [8–10]. This is one of the major factors that is usually put into consideration when nickel-based superalloys are being designed. Another challenge that superalloys often encountered in service is the build-up of thermal stresses [11]. These are often developed across the bulk volume of the materials due to uneven distribution of thermal energy. The thermal stresses are mostly due to the aggressive nature of the turbine environment and high-temperature/pressure of the steam/gas that is applied on the material. Therefore, the stresses can result to the distortion of components' microstructure [12, 13]. Hence, materials with good mechanical properties contribute in no small measure, to the efficiency and performance of the turbines

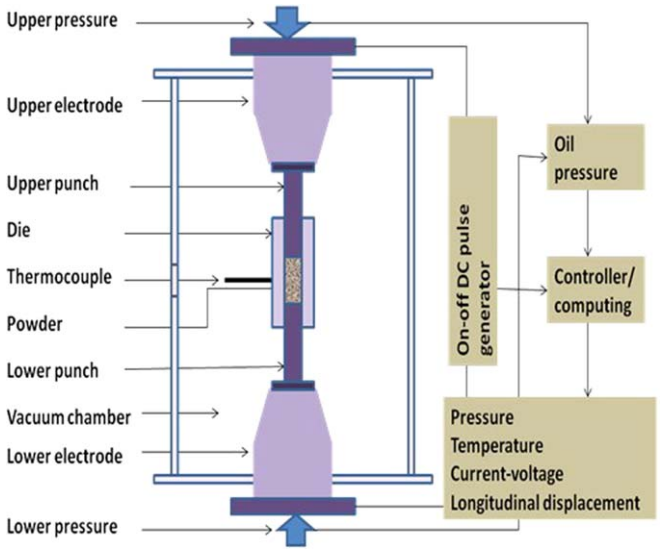

Figure 1. Spark plasma sintering setup [28].

and equally reduce the cost of maintenance. IN738LC has been widely used for high-temperature engineering applications. Primarily, it consists the gamma (γ) matrix phase (Ni) and the precipitate gamma prime (γ'-Ni_3(Al, Ti)) intermetallic phases [14]. These two phases are usually known to be a coherent face centered cubic (fcc) crystal structure. They are the phases that partly responsible for the hardness strength and increased melting temperature of the alloy.

However, the needs to keep improving the properties of IN738LC alloy, such as the material and mechanical properties, cannot be overemphasized [15–17]. Therefore, a careful selection of the fabrication route that is flexible to micro-constituent and structural features manipulations is imperative. The microstructure features include the grain formation (size, shape and orientation), material's densification, defects, micro-segregations and other microstructural features. Various metallurgy methods for fabricating superalloys have been widely reported. Some of these include the conventional melting and casting techniques (induction furnace melting and investment casting method, having its end-product as bars, metal sheets and other desired shapes). However, microsegregations, impurities, inclusions, formation of freckles, pores and some other defects are unavoidable in the conventional methods [18]. To circumvent the limitations that is often encountered in the conventional processing method, powder metallurgy (PM) has been research to be a better alternative. PM have been appreciably patronized by metallurgist due its advantages over the conventional methods such as, ability to produce components of infinite complexities and to form a near net shape component [19, 20]. Some of the methods that emanated from PM include metal injection moulding (MIM), microwave sintering (MW), hot isostatic press (HIP), laser sintering/laser melting and spark plasma sintering techniques [21–26]. The breakthrough that yielded considerable results in the application of powder metallurgy technology, started in the early 1960s [27] and subsequently gained attention up to this present time. SPS method involved, using a pulsed direct electrical current of low voltage and uniaxial force (under low atmospheric pressure), for powders consolidation. It is a fast sintering process for compacting and consolidating metallic and non-metallic powders. The schematic diagram of spark plasma sintering technology used in this study is presented in figure 1.

SPS technology is a processing route that consolidates and densifies powders in one-step of operations. The diffusion mechanism is characterized by heating and rapid cooling of the fabricated material in a sequential order. By so doing, the densification process is hastened, and grain growth formation is reduced. Some of the benefits of using SPS includes grain refinement, homogenous distribution of elemental composition, near-uniform heat distribution during sintering, formation and even distribution of secondary phase precipitates (for alloy prone to precipitate formation or intermetallic phase formation) [29]. In addition, some of the advantages of SPS technology over the isostatic press, hot press, microwave sintering and atmospheric furnace in PM include micro-segregation elimination, porosity reduction, fabrication of materials with superior mechanical properties, fabrication of components to dimensional precision and production of materials with good surface-finish properties [30]. Relatively, a few numbers of studies have been carried out on the fabrication of nickel-based superalloy using SPS, but since its existence, it is still at the laboratory stage [31]. More importantly, few reports are available on the use of SPS in fabricating IN738LC superalloy. However, effort is ongoing to establish a documented processing data that can be adapted when full knowledge of the industrial application of SPS is

Table 1. W % of IN738LC composition.

Material	Ni	Cr	Co	Ti	Al	W	Ta
Weight (%)	64.58	16	8.3	3.4	3.4	2.6	1.72

established. Thus, the objective of this work is to investigate the densification and microstructural characteristics of spark plasma sintered IN738LC superalloy by optimizing the sintering temperature.

2. Experimental procedure

An experimental investigation was carried out to evaluate the influence of SPS processing temperature on the microstructure of IN738LC superalloy. Seven different individual metallic powders were combined to form a nickel-based superalloy known as Inconel 738LC [11]. A Ni powder (TLS-Technik Gmbh, 99.5%) was used as the base material with a particle size range between 45–90 μm, in addition with Aℓ powder (TLS-Technik Gmbh, 99.8%) with a particle size of 25 μm. Other metallic powders include Co, Ta, W, Ti and Cr, with particle sizes below 45 μm. Ta, W and Ti were supplied by Sigma Aldrich, while Alfa Aesar supplied the Co and Cr powders, which have an elemental purity of 99.9%. All the starting powders were spherical. The powders were accurately weighed to have a desired stoichiometric composition in accordance with IN738LC standard [11]. The percentage weight fraction of the alloy compositions is summarized in table 1. A digital weighing balance was used to carefully weigh each powder to the desired percentage composition and poured into a tubular mixer for pre-alloying. At first, the powders were pre-alloyed for a period of 16 h at 96 rpm in the mixer. A ball-to-powder ratio of 10:1 was used for the pre-alloyed process in order to ensure even distribution of powder particle within the matrix. This was done in a dry environment and the balls used were tungsten. The balls were carefully rinsed with ethanol to remove impurities on the surface and allowed to dry for a period of 30 min. The balls and the powders were poured into an air-tight plastic bottle and placed in the holding chamber of the mixer. Afterwards, the machine was covered and switched on. At the completion of the mixing procedure, the green powder was quickly transferred into the prepared graphite die.

The variation in the particle sizes of the elemental powders (compositions) is targeted at improving the densification and microstructural evolution during powder consolidation by using a spark plasma sintering process [32]. The feedstock powders (individual elements) were of a different size range; the shapes of all the powders were spherical with the biggest particle diameter size less than or equal to 90 μm for Ni. The least elemental powder particle size diameter is for the Al element, which is less than or equal to 25 μm. The other elemental powders particle sizes (Ta, Cr, W, Ti, Co) were between 3–45 μm and were all spherical in shapes. Green powder of 59.54 g was poured in a 40 mm diameter graphite die for each round of sintering to obtain a dense sample of 6 mm thickness and a diameter of 40 mm size. The die used have an internal diameter of 40 $\pm$ 0.05 mm, external diameter of 60 $\pm$ 0.1 mm and a height of 48 mm. The green powder has a theoretical density of 7.894 g cm^{-3} as calculated by using equation (1).

$$TD = \frac{1}{\left(\frac{\text{wt\% of element } A}{\text{density of sample } A}\right) + \left(\frac{\text{wt\% of element } B}{\text{density of sample } B}\right) + \ldots + \left(\frac{\text{wt\% of element } n!}{\text{density of sample } n!}\right)} \quad (1)$$

where TD is the theoretical density.

The sintering was done in a spark plasma-sintering machine (model HHPD-25 from FCT Germany). The vacuum atmosphere was maintained at 0.5 mbar, and this is necessary to ensure minimal oxygen contamination on the samples during sintering. Sintering procedure includes inserting a graphite foil (0.3 mm thick) in between the graphite die and the green powder to avoid direct contact of the powder with the graphite punch and die. The graphite foil prevents the occurrence of a chemical reaction between the powder and the die. This also ensures easy removal of the sintered samples from the mould after sintering. The green powder was cold compacted inside the mold (die and punches) using LAB mini pressing machine at a pressure of 10 MPa for a period of 2 min. Thereafter, the graphite die, filled with green powder was placed in the heating chamber of the furnace. Sintering of the powders followed at four different temperatures (i.e. 900, 1000, 1100 and 1200 °C), while other parameters are kept constant (i.e., pressure of 50 MPa, holding time of 5 min and heating rate of 100 °C min^{-1}). A pressure of 50 MPa was applied at the beginning of the sintering and was unchanged until after the soaking time of 5 min. The samples were cooled at the rate of 100 °C min^{-1} in the furnace before they were removed.

The sintering temperature was closely monitored and recorded with the optical pyrometer, which was placed in the SPS setup at 3 mm distance from the top of the sample surface. After the sintering process, the samples were removed and sand-blasted to remove the carbon deposited on the sample surface through the

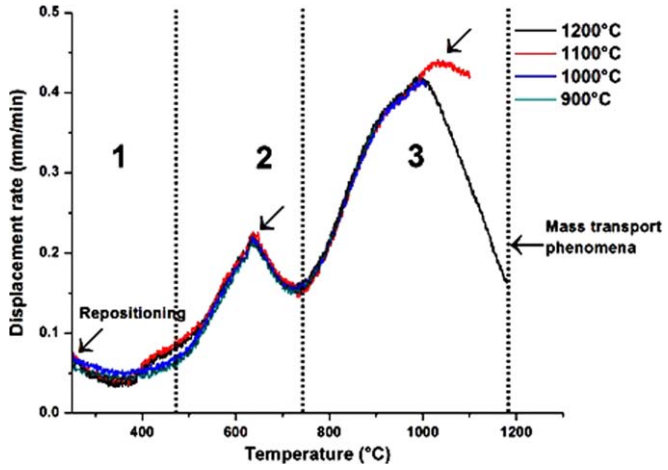

Figure 2. Displacement rate versus temperature for IN738LC sintered at 900, 1000, 1100 and 1200 °C.

graphite foil used for insulation during sintering. The density of the sintered samples was measured by following the Archimedes' method, using distilled water as a wetting liquid in a digital weighing balance. Metallographic preparation of the sample was conducted by pre-grinding with different grades of SiC emery paper [33]. This was followed by polishing. The samples were etched in a solution consisting of 2 g $CuCl_2$, 50 ml HCl, 25 ml HNO_3 and 200 ml H_2O. The phases present and morphological analyses of the microstructure were examined using a Falcon 500 series polarizing optical microscope (POM) and a JEOL JSM-7600F scanning electron microscope (SEM). The SEM was incorporated with an EDS detector and INCA X-Stream2 pulse analyzer software. For the microstructural analysis, the INCA analyzer software in the SEM machine was set at 70 s acquisition time and at a processing time of 2 s. The POM was used to measure the grain size and this procedure follows the ASTM E112 standard by using Contrast Method (Brightfield Reflective light), Objective (EC Epiplan-Neofluar 20x/0.5 HD DIC M27), Camera (AxioCamICc5) and Scaling (0.2738 Micrometer /Pixel) [34]. The phases formed in the sintered samples were characterized using a PANalytical Empyrean x-ray diffraction (XRD) machine, which is a model with Cu Kα radiation. The XRD spectra were analyzed with an X'Pert HighScore plus software. The material hardness was characterized using a Vickers microhardness tester (Future-tech) at a load of 500 gf (5.0 N) and a holding time of 10 s. The hardness test was conducted five times at different positions. The hardness results presented in this study are the arithmetic mean of the five successive indentations.

3. Results and discussion

3.1. Densification behaviour of IN738 powders sintered at 900 °C–1200 °C

The displacement rate patterns developed during spark plasma sintered IN738LC superalloy is shown in figure 2. The patterns were formed as a result of the application of axial force which was exerted on the powder through the piston, coupled with the sintering temperature applied. The alloys were sintered at four different temperatures between 900°C–1200°C. The densification occurrence, which is the changes in the thickness (shrinkage) of the samples by powder consolidation, was recorded. According to the displacement rate curve, three stages were observed. The first stage represents the repositioning of the particles within the bulk volume of the component due to pressure. The second stage shows the area of localized deformation at the contact points, while the peaks at this point were observed at temperatures of between 610°C–670°C. This is where the energy supplied, conquered the opposing energy of the particles (recrystallization start). Lastly, the third stage shows the area where the bulk deformation of the particles occurred [35].

The sintering system that was employed in this experiment was calibrated to operate with a high-temperature reading pyrometer. The temperature activity before attaining 250 °C was not read nor recorded by the system. Thus, the system recorded the situation of operation from 250 °C and above. From figure 2, it can be observed that the first peak for all the samples started at 250 °C. This indicates that prior to this stage, there was a densification activity. The trajectory curve observed for the four samples (sintered at 900, 1000 and 1100 and 1200 °C) is similar. The curves were seen to overlap as they progress with increasing sintering temperature. A sharp increase in the punch displacement rate beyond 760 °C was observed. This is due to the thermal softening of the compact. The trajectory of the displacement curve for the sample sintered at 1200 °C, follows a depression path at a temperature around 1000 °C. The impact of the sintering temperature on the densification behaviour of the samples was observed from the displacement rate recorded. The least total displacement rate was obtained

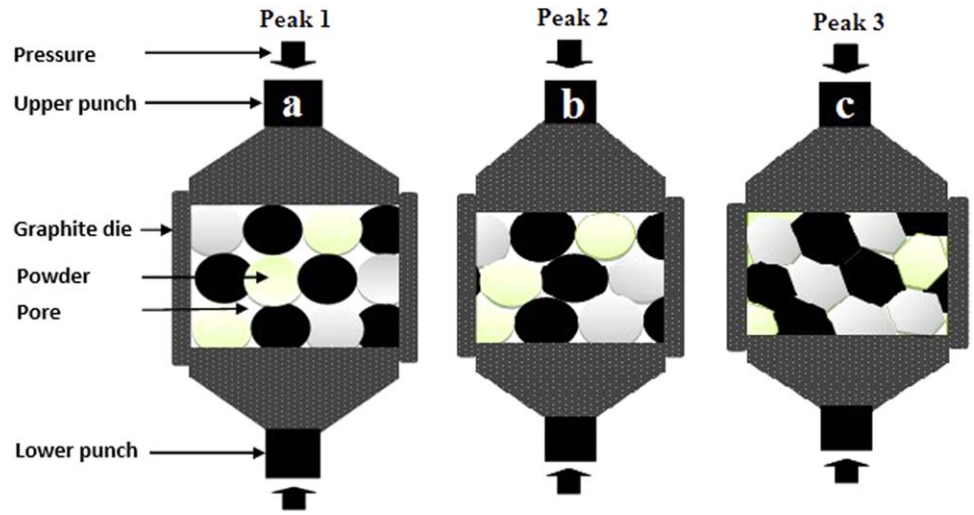

Figure 3. Schematic representation powder consolidation: (a) powder consolidation at stage 1, showing particle rearrangement (b)particles consolidation at stage 2, showing local deformation (c) Stage 3, shows the developed grains after sintering with bulk deformation.

at 900 °C (0.37 mm min^{-1}), while the highest was obtained at 1100 °C (0.44 mm min^{-1}, 18.9% increment). The total displacement rate for the sample sintered at 1200 °C was 0.42 mm min^{-1}. However, between the sample sintered at 1200 and 1100 °C, there is a difference of 0.02 mm min^{-1} displacement rate (4.5% difference).

The lower displacement rate obtained, confirmed the detrimental effect of low sintering temperature on densification. This was evident in the relative density and the microhardness value obtained. The difference in the displacement rate of sample sintered at 1100 and 1200 °C, which is marginal (4.5% difference), suggest that the two temperatures are good for the densification of IN738LC alloy. The phenomena that occurred in the three stages can be explained thus: as was reported in figure 2, the first stage implies that there was a prior rearrangement of powder particles due to the pressure applied. Stage two implies that there was limited particle deformation, and it is the point where necking formation started (localized deformation), which further increased in the packing. This indicated that deformation began at this stage, mainly at the surface before progressing to the core of the sample. This observation conforms to the results reported by Song *et al* [36]. The third stage signifies bulk deformation of the particles leading to grain formation; this is an indication that plastic deformation of the particles had occurred, which extended to the core of the alloy. The two displacement rate peaks (stages 2 and 3) shown in figure 2, therefore portray the occurrence of plastic deformation of the powder particles under concurrent application of heat and pressure. Furthermore, the transition process of the powder particles to grains from particle rearrangement to local deformation and bulk deformation is shown as a schematic in figure 3.

Consequently, the amplitude of the two peaks (stages 2 and 3) and the degree of the densification involved, are then linked, intrinsically to the magnitude of the deformation of the alloy, since a sharp peak was observed. However, a slightly stretched peak was observed at the third stage, which can be interpreted as an expansion of the deformation into the core of the sample, resulting in large densification. Even though the peak suggests large deformation, the sample has not been sintered yet, since a progression of the curve was still obvious, although it has been densified. The obvious descending of the displacement rates curve signifies a fully dense and sintered specimen, which means an effective consolidation of the specimen has been performed. At this point, it may be concluded that mass transport phenomenon had occurred, a concept responsible for necking and grain growth. Hence, the reason for a continuous decrease in the displacement rate curve because the powders had already been densified [30]. In summary, temperature accelerates deformation, thereby causing initiation of neck growth at the first stage of the sintering cycle. The second stage experienced thermal softening of the compact due to adiabatic heating and dynamic recrystallization. The third stage experienced high dislocation motion due to thermal stress. As a result, bulk deformation and porosity annihilation occurred. This allowed densification as a response to sintering stress.

3.2. Microstructure and EDX characteristics of IN738LC superalloy

The optical and SEM micrographs, showing the microstructures of sintered IN738LC alloys were represented in figures 4(a)–(g). The optical images of the etched sample are shown in figures 4(a), (c), while figures 4(d)–(g) represent the SEM images. The optical images were that of the specimen sintered at 1200 °C, taken at different

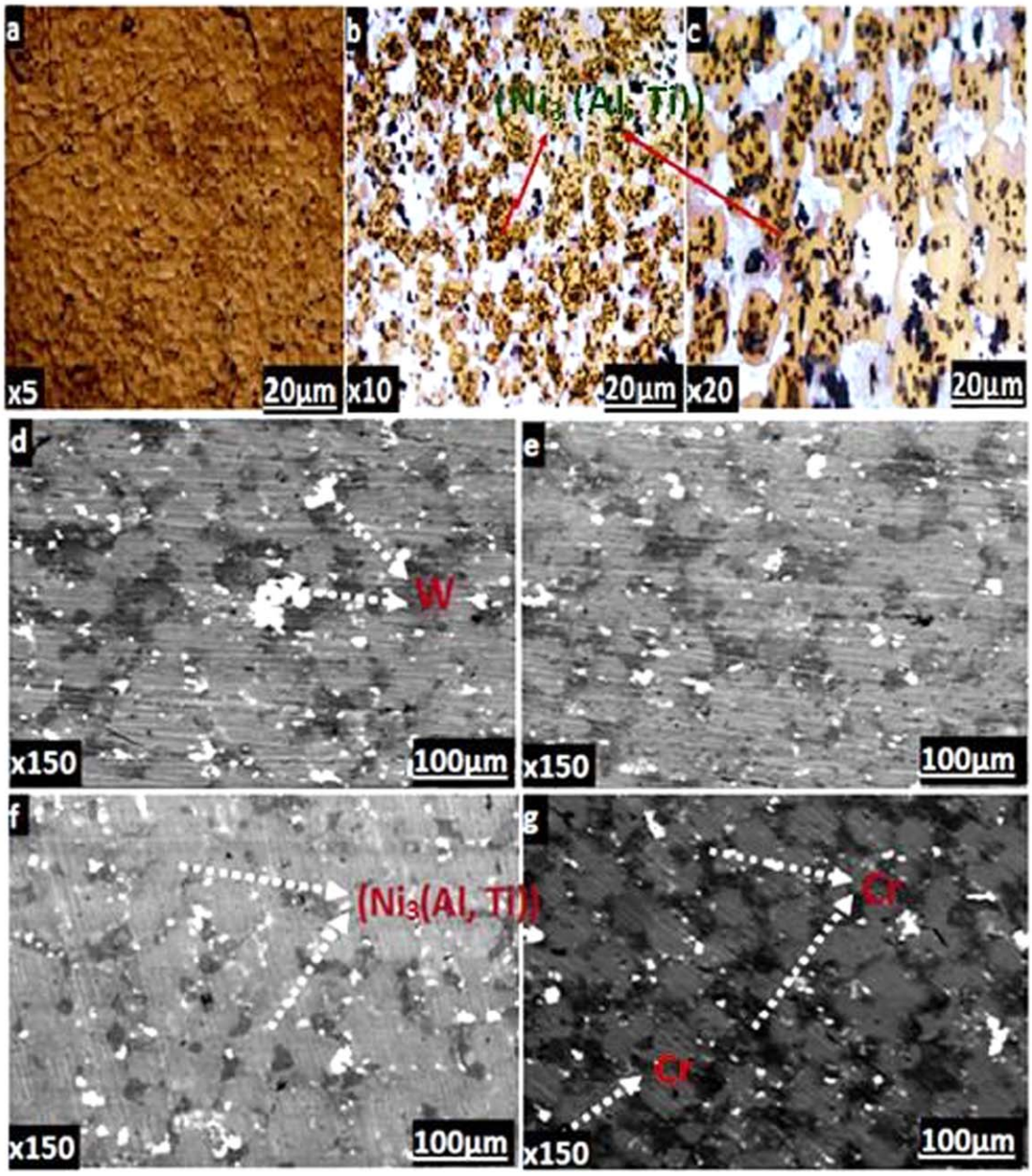

Figure 4. POM microstructure (a)–(c) of IN738LC sintered at 1200 °C and SEM microstructure (backscattered) of sintered specimen at different temperatures (d) 900 °C (e) 1000 °C (f) 1100 °C (g) 1200 °C.

magnifications and the SEM images were for all the four samples, d (900 °C), e (1000 °C), f (1100 °C) and g (1200 °C), respectively. From figure 4(a), a rough surface was observed with black patches, dotted scantily across the surface of the sample; this was observed in different sizes and can be presumed to be pores located between the grains, although not so obvious on a bigger magnification. Island of white patches was equally observed in figures 4(b)–(c), which was later confirmed by the elemental mapping graph in figure 5, to be a chromium-rich zone. The chromium-rich spots were strategically located at the grain boundaries of the $\gamma + \gamma'$ matrix. This is an indication that it was evenly distributed across the samples. However, this is not surprising because, after the nickel element, chromium was the next element that is present in large quantity (16%). The pre-alloying of powders for 16 h ensures the homogenization of the ad-mixed powder, which is what was evident on the microstructure.

In addition, an intermetallic phase was observed, this was later distinguished by using XRD machine to analyze the phases and this is reported in section 3.4. These are phases known to poses high strength properties, with FCC structure. This suggests that the alloy will have high stability strength at both elevated and room temperature. This agrees with some previously reported works [37, 38] and it is designated with brown colour on the micrograph, with some black patches in between. A close observation of the SEM images in figures 4(d)–(g) shows that the grains were of different orientations and sizes. This is of great benefit to the sintered alloy as its

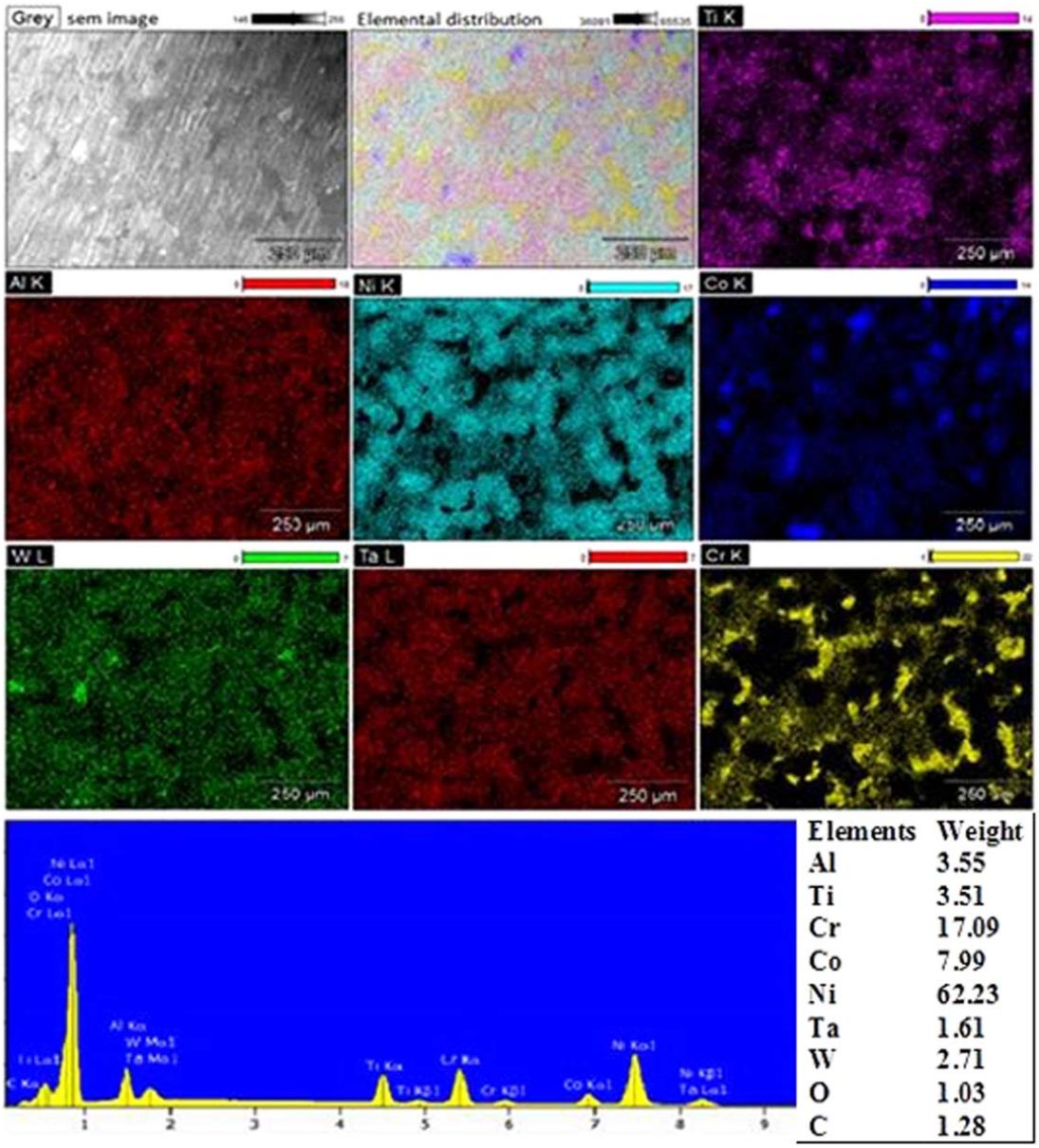

Figure 5. EDS mapping and element distribution of IN738LC alloy sintered at 1200 °C.

suggesting that the samples attained good densification. Furthermore, the BSC-SEM images show very faint pores within the bulk volume of the sintered samples. All these are of great advantage, as they contributed to the quality of the densification produced. The light grey area is the $\gamma + \gamma'$ (primary matrix and secondary intermetallic) zone. The dark grey area, as seen in the micrograph in figures 4(d)–(g) and confirmed by the EDX in elemental mapping graph in figure 5, is the chromium-rich zone. The white spot on the SEM-BSC images represents the un-dissolved tungsten that is known to be a solid solution hardening element. It has a high density and melting temperature point. The oxygen and carbon observed on the EDX graph are trace elements that are present as a result of material handling during the process of pouring powders into the graphite die. Figure 5 shows the elemental distribution of IN738LC alloy which was sintered at 1200 °C. The precipitation of Co and Cr was observed, including the homogenous distributing alloying elements.

3.3. Grain size

Figure 6 represents the POM image annotations of the sintered samples, measuring the grain sizes and the comparison of average grain size of the samples with respect to sintering temperature. Observation shows that there was little difference in the average grain size (AVG) of the four sintered samples, with the highest AVG at 900 °C, which is around 9.5 μm. The least was at 1100 °C, and 1200 °C, having 8 μm as their AVG. It is apparent that an increase in temperature leads to a marginal decrease in the average grain size, although all the samples were processed at the same holding time of 5 min. This may be due to the plasticity dynamics that occurred as the

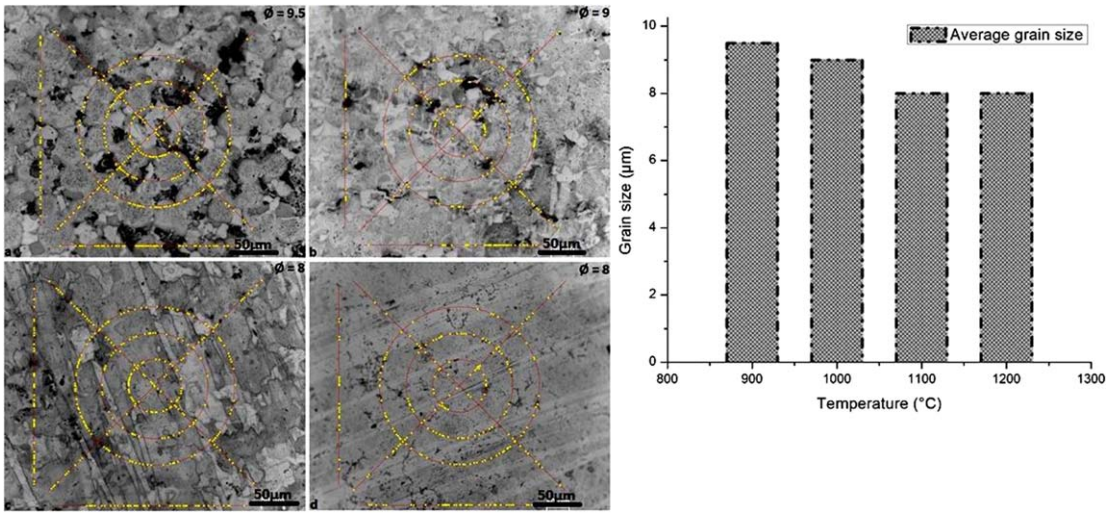

Figure 6. Annotation images and Average grains size measurement of IN738LC sintered at 900.

sintering temperature increases. The plasticity occurrence enables grain boundary formation and ensured that the pores were close within the grain leading to shrinkage and marginal decrease in the average size of grain. Guillaume and Christian [39] studied the sintering behaviour of zirconia. They investigated the mechanism that controlled densification and sintering path and observed that 5 min soaking time is not sufficient for grain growth. The grain size of the materials sintered for 5 min was the same. They further confirmed that considerable grain growth formation occurred after the soaking time was increased to 15, 60 and 180 min respectively. Therefore, we believed that the 5 min holding time that was used in our study could only produce marginal changes in grain size and the time may not be sufficient for extensive grain growth. In comparison with the hardness property, the bigger the grain size, the lower the hardness. This is in line with the Hall-Petch relationship. In addition, the solid solution strengthening elements of chromium and tungsten as seen in the micrograph might be part of what contributed to the hardness property. In figure 9, the relationship between grain size and hardness property is clearly, displayed.

3.4. X-ray diffraction analyses

XRD analysis of the sintered IN738LC alloy samples produced at different sintering temperatures of 900, 1000, 1100 and 1200 °C with the peaks of phases formed are shown in figure 7. The precipitated secondary γ' intermetallic phase (Ni_3Ti, Ni_3Al) was the predominant phase observed in all the sintered samples. This occurred at five different angles 2θ peaks. In addition, some other phases and elements present include the primary γ phase (Ni) matrix, Ta and Cr_2 elements. Ta, which is one of the solid solutions strengthening elements was only visible in the samples sintered at 900 and 1000 °C at a diffraction angle close to $2\theta = 90°$. This dissolved into the matrix at a higher temperature above 1000 °C. The Ta peak intensity was nearly invincible as shown in figure 7. At 2θ angles of 45, 52 and 77°, it was observed that the peaks of γ and γ' phases overlapped in their formation. A broadening of peaks with reduced intensity was observed as the sintering temperature increases. In a similar study, conducted by Sarkar *et al* [40], it was reported that the peaks obtained for the γ matrix and the γ' intermetallic phase from the XRD analyses overlapped. In nickel-based superalloys, different types of oxide phases may occur, especially when the alloy is subjected to an oxide environment. Therefore, the presence of Cr_2 will certainly help in the formation of the protective oxide layer. Hence, the reaction of Cr_2 with oxygen will lead to the formation of a protective layer on the surface of the bulk material. It was also observed that the intensity of the peak at a 2θ angle of 45°, which is the dominant point where γ and γ' occurred and overlapped, reduces with an increase in sintering temperature. This is suggesting that dissolution of the two precipitated phases occurred as the sintering temperature increases.

3.5. Microhardness relationship with sintered density and grain size

Figure 8 shows the relative density of the sintered samples against the hardness property. It was observed that the relative densities of the materials have a great influence on their mechanical properties. The data in figure 8 revealed that the relative density values obtained from the density measurement using Archimedes ' principle increased and the microhardness values also increased with increasing sintering temperature. The microhardness values of the sintered IN738LC alloys increased from 287 Hv to 362 Hv, as the relative density increased from 90% to 98% respectively. The highest relative density was obtained at 98%, and it was evident

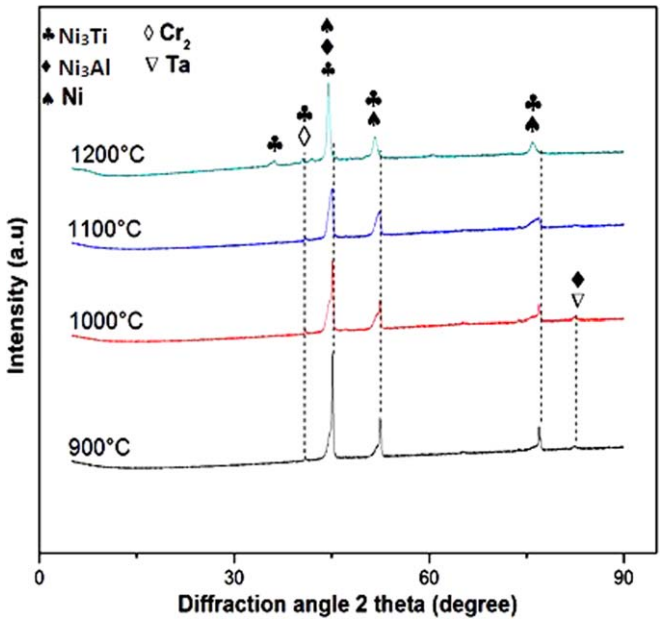

Figure 7. XRD patterns of the sintered IN738LC alloy at 900, 1000, 1100, and 1200 °C.

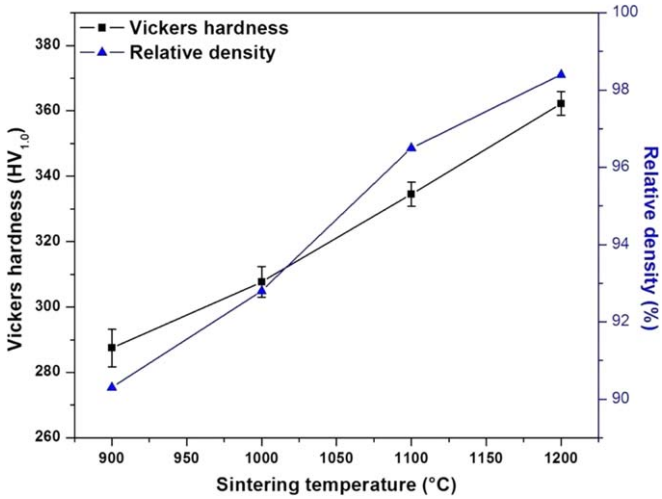

Figure 8. The relative density and hardness of the sintered samples at different temperatures.

from the microstructures obtained for this alloy, minimal pores could be seen on the micrograph. The increase in densification with the increasing sintering temperature can be attributed to the presence of smaller grain size and the presence of solid solution strengthening hard element (W, Cr), as it was observed from figure 4. The formation of γ' intermetallic phase within the matrix, is also a factor that can is responsible for the increase in the hardness values [13], although not quantified. Figure 9 shows the relationship between the microhardness, grain size and the sintering temperature. It was observed that the hardness values increased with a marginal decrease in grain size and with increasing sintering temperature. The alloy with the least average grain size, sintered at 1100 and 1200 °C, have their corresponding hardness value to be 334 and 362 Hv respectively. The alloy sintered at 900, and 1000 °C have an average grain size of 9.5 and 9 μm, with their corresponding hardness value as 287 Hv and 308 Hv respectively. The increase in the hardness values at high sintering temperature may be due to the influence of the individual hardness strength of the elements that formed solid solution strengthened phases. Therefore, relating the Hall-Petch relationship to our observation, it could be noticed that the bigger the grain size, the lower the hardness strength. Consequently, a high sintering temperature can hasten the densification and consolidation of metallic powders.

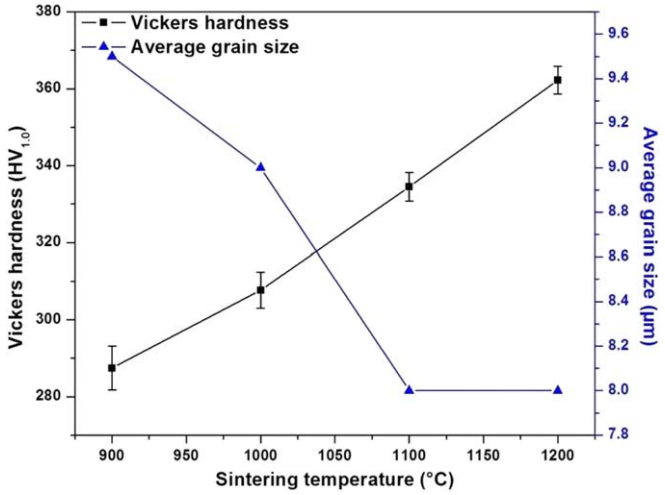

Figure 9. Relationship between microhardness and the grain size in the sintered samples.

4. Conclusion

In this work, the densification, microstructure, and microhardness of spark plasma sintered Inconel 738LC superalloy, sintered at 900, 1000, 1100 and 1200 °C temperature was investigated and characterized by using SEM, XRD, Vickers microhardness tester. Based on the results, conclusions can be drawn as follow:

(1) As the sintering temperature increases, the densification of the sintered alloys increases. This is also corroborated by the gradual increase in the displacement rate with respect to increasing sintering temperature. The recrystallization temperature peak (stage 2) conforms to the 0.4*Tm* of the nickel-based superalloys in general. In this work, the 0.4*Tm* of IN738LC was around 650 °C, and the maximum densification attained was at 1200 °C, which was approximately 98%.

(2) The morphology of the sintered sample contained, the primary γ-phase, secondary γ'-phase and W, Cr solid solution strengthening elements. Coherent γ' precipitate was observed to be inherent within the matrix and can be said to be uniformly distributed within the γ-matrix. Pores were less obvious within the morphology; there was little difference in the average grain size of the four sintered samples, while the hardness property increased with a decrease in the grain size.

(3) The sample sintered at 1200 °C, possessed superior hardness property, the Vickers microhardness value was 362 at $Hv_{1.0}$, with an average grain size of 8 μm. The presence andthe distribution of precipitated intermetallic phases, which formed solution hardening and as seen in the XRD spectra contributes to the increased hardness value.

Acknowledgments

This work is funded by the Research and Innovation Directorate of Tshwane University of Technology and supported, in part, by the:Department of Mechanical Engineering, Mechatronics and Industrial Design, Institute for NanoEngineering Research (INER), Department of Chemical, Metallurgical and Materials Engineering and the Faculty of Engineering and Built Environment of the Tshwane University of Technology, Pretoria, South Africa.

ORCID iDs

O F Ogunbiyi https://orcid.org/0000-0002-6260-450X
O T Adesina https://orcid.org/0000-0002-1840-8691

References

[1] Shi Z-X *et al* 2015 Effects of Cr content on microstructure and mechanical properties of single crystal superalloy *Trans. Nonferr. Metals Soc. of China* **25** 776–82
[2] Li Z and Mills K C 2006 The effect of γ' content on the densities of Ni-based superalloys *Metallurg. Mats. Trans.* B **37** 781–90

[3] Wang L *et al* 2015 Effect of surface roughness on the oxidation behavior of a directionally solidified Ni-based superalloy at 1,100 °C *Acta Metallurg. Sinica (Eng. Letts.)* **28** 381–5
[4] Liu G-M *et al* 2017 Corrosion behavior of the Ni–Cr–Fe base superalloy GH984G in a synthetic coal ash and flue gas environment *Acta Metallurg. Sinica (Eng. Letts)* **30** 863–8
[5] Akca E and Gürsel A 2015 A review on superalloys and IN718 nickel-based INCONEL superalloy *Period. Eng. Nat. Sci.* **3** 1–13
[6] Zou J-W *et al* 2018 Characterization of interfacial bonding mechanism for graphene-modified powder metallurgy nickle-based superalloy *Acta Metallurg. Sinica (Eng. Letts)* **31** 753–60
[7] Guo Y, Wang B and Hou S 2013 Aging precipitation behavior and mechanical properties of Inconel 617 superalloy *Acta Metallurg. Sinica (Eng. Letts)* **26** 307–12
[8] Barelli L and Ottaviano A 2015 Supercharged gas turbine combined cycle: an improvement in plant flexibility and efficiency *Energy* **81** 615–26
[9] Ambec S and Crampes C 2012 Electricity provision with intermittent sources of energy *Resce. Energy Eco.* **34** 319–36
[10] Keatley P, Shibli A and Hewitt N 2013 Estimating power plant start costs in cyclic operation *App. Energy* **111** 550–7
[11] Rani S, Agrawal A K and Rastogi V 2017 Failure analysis of a first stage IN738 gas turbine blade tip cracking in a thermal power plant *Case Stud. Eng. Fail. Anly.* **8** 1–10
[12] Li R *et al* 2002 Isolation and determination for δ, γ' and γ'' phases in inconel 718 alloy *Scrt. Mat.* **46** 635–8
[13] Ma S *et al* 2018 Effects of temperature on microstructure and mechanical properties of IN718 reinforced by reduced graphene oxide through spark plasma sintering *J. Alloy. Compd.* **767** 675–81
[14] Maleki V, Omidvar H and Rahimipour M-R 2018 Influences of gap size and cyclic-thermal-shock treatment on mechanical properties of TLP bonded IN-738LC superalloy *Trans. Nonferr. Metals Soc. of China* **28** 920–30
[15] Wang X *et al* 2017 Microstructure and yield strength of SLM-fabricated CM247LC Ni-superalloy *Acta Mat.* **128** 87–95
[16] Makena M I *et al* 2017 Effect of sintering parameters on densification, corrosion and wear behaviour of Ni-50Fe alloy prepared by spark plasma sintering *J. Alloy Compd* **699** 1166–79
[17] Wu J *et al* 2017 Microstructural characterization and phase separation sequences during solidification of Ni 3 Al-based superalloy *Acta Metallurg. Sinica (Eng. Letts)* **30** 949–56
[18] Kushan M C *et al* 2012 ALLVAC 718 Plus™ superalloy for aircraft engine applications *Recent Advances in Aircraft Technology* (Rijeka: InTech)
[19] Kirka M M *et al* 2017 Solidification and solid-state transformation sciences in metals additive manufacturing *Scrt. Mat.* **135** 130–4
[20] Gibson I, Rosen D W and Stucker B 2010 *Design for Additive Manufacturing, in Additive Manufacturing Technologies* (Boston, MA: Springer) pp 299–332
[21] Jia C-L, Ge C-C and Yan Q-Z 2016 Innovative technologies for powder metallurgy-based disk superalloys: progress and proposal *Chin. Phy.* B **25** 026103
[22] Mishra R R and Sharma A K 2016 Microwave–material interaction phenomena: heating mechanisms, challenges and opportunities in material processing *Compt. Part A: App. Sci. Manuf.* **81** 78–97
[23] Chang L *et al* 2017 Preparation of hot-isostatic-pressed powder metallurgy superalloy Inconel 718 free of prior particle boundaries *Mat. Sci. Eng.* A **682** 341–4
[24] Sadowski M *et al* 2016 Optimizing quality of additively manufactured Inconel 718 using powder bed laser melting process *Add. Manuf.* **11** 60–70
[25] Yamanoglu R *et al* 2014 Characterisation of nickel alloy powders processed by spark plasma sintering *Powd. Metallurg.* **57** 380–6
[26] Albert B, Völkl R and Glatzel U 2014 High-temperature oxidation behavior of two nickel-based superalloys produced by metal injection molding for aero engine applications *Metallurg. Mats Trans.* A **45** 4561–71
[27] Tsutsui T 2012 Recent technology of powder metallurgy and applications *Hitachi Che. Tech. Rep.* **54** 12
[28] Ogunbiyi O *et al* 2019 Microstructural characteristics and thermophysical properties of spark plasma sintered Inconel 738LC *Int. J. Adv. Manuf. Tech.* **104** 1425–1436
[29] Ghosh N and Harimkar S 2012 Consolidation and synthesis of MAX phases by Spark Plasma Sintering (SPS): a review *Adv. Sci. Tech. Mn + 1axn Pha.* (Amsterdam: Elsevier) pp 47–80
[30] Diouf S and Molinari A 2012 Densification mechanisms in spark plasma sintering: Effect of particle size and pressure *Powd. Tech.* **221** 220–7
[31] Mamedov V 2002 Spark plasma sintering as advanced PM sintering method *Powd. Metallurgy* **45** 322–8
[32] Shongwe M B *et al* 2015 Effect of sintering temperature on the microstructure and mechanical properties of Fe–30%Ni alloys produced by spark plasma sintering *J. Alloy Compd* **649** 824–32
[33] Pérez-González F, Garza-Montes-de Oca N and Colás R 2014 High temperature oxidation of the Haynes 282© nickel-based superalloy *Oxid. Metals* **82** 145–61
[34] Standard, A., E112-13 2013 Standard Test Method for Determin ing Average Grain Size *West Conshohocken PA*, pp 1-28 www.astm.org
[35] Bayode B *et al* 2017 Densification and micro-structural characteristics of spark plasma sintered Ti-Zr-Ta powders *Powd. Tech.* **321** 471–8
[36] Song X, Liu X and Zhang J 2006 Neck formation and self-adjusting mechanism of neck growth of conducting powders in spark plasma sintering *J. Ame. Ceram. Soc.* **89** 494–500
[37] Jalilvand V *et al* 2013 Microstructural evolution during transient liquid phase bonding of Inconel 738LC using AMS 4777 filler alloy *Mats Charact.* **75** 20–8
[38] Rosenthal R and West D R F 1999 Continuous γ' precipitation in directionally solidified IN738 LC alloy *Mats. Sci. Tech.* **15** 1387–94
[39] Bernard-Granger G and Guizard C 2007 Spark plasma sintering of a commercially available granulated zirconia powder: I. Sintering path and hypotheses about the mechanism (s) controlling densification *Acta Mat.* **55** 3493–504
[40] Sarkar A *et al* 2008 Lattice misfit measurement in Inconel 625 by x-ray diffraction technique *Int. J. Mod. Phy.* B **22** 3977–85